

Characterization and active cancellation of power-line-induced motional-mode frequency noise in a trapped-ion system

Jaehun You^{1,2,3}, Jiyong Kang^{1,2,3}, Kyunghye Kim^{1,2,3}, Wonhyeong Choi^{1,2,3}, and Taehyun Kim^{1,2,3,4,5,*}

¹Department of Computer Science and Engineering, Seoul National University, Seoul, 08826, Republic of Korea

²Automation and Systems Research Institute, Seoul National University, Seoul, 08826, Republic of Korea

³NextQuantum, Seoul National University, Seoul, 08826, Republic of Korea

⁴Institute of Computer Technology, Seoul National University, Seoul, 08826, Republic of Korea

⁵Institute of Applied Physics, Seoul National University, Seoul, 08826, Republic of Korea

*taehyun@snu.ac.kr

ABSTRACT

The stability of motional-mode frequency is essential for realizing high-fidelity quantum gates in trapped-ion quantum computing. While broadband Gaussian noise has been extensively studied and mitigated using pulse shaping techniques, the impact of coherent periodic noise has remained largely unexplored. Here we report a systematic investigation of 60-Hz power-line noise and its effect on the secular frequencies of a single $^{171}\text{Yb}^+$ ion. Using spin-echo Ramsey spectroscopy, we characterize the amplitude and phase of the resulting secular-frequency modulation and validate this characterization via passive phase correction of the Ramsey sequence. Building on this, we implement active cancellation by injecting a compensation tone into the set-point of a PI controller that stabilizes the trap RF drive amplitude. A phasor-fitting procedure optimizes the amplitude and phase of the compensation signal, enabling near-complete suppression of the 60-Hz component. With active cancellation engaged, the coherence time of a radial motional mode is extended from approximately 10 ms to 35 ms, consistent with the limit set by motional heating. Our results provide both a clear characterization of periodic motional-mode noise and a practical framework for its suppression in trapped-ion quantum computing platforms.

Introduction

In trapped-ion quantum computers, the shared motional modes of the ions provide the quantum bus that mediates multi-qubit entangling gates^{1–4}. The long-term stability of these modes is therefore a central requirement for scalable, high-fidelity quantum logic operations^{5–7}. It is likewise essential for continuous-variable quantum computing and bosonic-encoding protocols that rely on precise phase-space control and phase accumulation of motional states^{8,9}.

In many cases, dephasing in trapped-ion systems is modeled as stationary Gaussian noise and analyzed using the filter-function framework, where a control sequence acts as a frequency-domain filter on the noise power spectral density, enabling both noise spectroscopy and the systematic design of dephasing-robust operations^{10–13}. More generally, this filter-function framework¹⁴ has been widely applied across diverse platforms, including nuclear magnetic resonance¹⁵, superconducting circuits^{16,17}, nitrogen-vacancy (NV) centers in diamond¹⁸, and semiconductor quantum dots¹⁹.

For motional modes in particular, frequency fluctuations are often characterized by a power spectral density^{20–22}. This spectral characterization has enabled substantial progress in mitigating dephasing from stochastic Gaussian noise through noise-robust control techniques such as pulse shaping¹³. However, trapped-ion experiments also face structured noise sources that are coherent and periodic, leading to deterministic modulation of the secular frequency with a well-defined phase relative to an external reference^{23,24}. Because the phase of such perturbations is not captured by a stationary noise power spectral density alone, a common practical workaround is to phase-synchronize each experimental shot to the underlying periodic reference.

A prominent example of such structured noise is power-line noise at 50/60 Hz, which is encountered across diverse platforms, including superconducting circuits²⁵, NV centers in diamond^{26,27}, and semiconductor quantum dots²⁸. In trapped-ion systems, power-line noise likewise constitutes a well-known structured perturbation that can limit qubit coherence via power-line-synchronous magnetic-field fluctuations²⁹; accordingly, it is common practice to synchronize each experimental shot to a fixed phase of the line cycle (line triggering) to reduce its impact^{30–33}. Building on this practice, several works have quantitatively characterized power-line-synchronous qubit-frequency modulation and demonstrated active cancellation

techniques to mitigate it^{34–36}. Motional-mode secular frequencies can exhibit analogous power-line-synchronous modulation through electrical pathways, for example via RF-drive amplitude pickup, and this has motivated the use of line-triggered operation in practice²³. Several works have further quantified this effect by characterizing the modulation²⁴. However, in contrast to the qubit case, practical methods for actively canceling line-synchronous secular-frequency modulation of motional modes appear to have received little attention to date.

In this work, we investigate the effect of 60-Hz power-line noise on the motional modes of a single trapped $^{171}\text{Yb}^+$ ion, and we develop and demonstrate a systematic workflow for its characterization and active cancellation. By extracting both the amplitude and phase of the induced secular-frequency modulation, we implement an active noise-cancellation scheme based on direct feedforward injection into the trap control system. Our approach not only suppresses the dominant periodic component but also provides a practical template for identifying and compensating structured, coherent noise in trapped-ion systems. To the best of our knowledge, this constitutes the first experimental active cancellation of periodic motional-mode noise in a trapped-ion system, highlighting both its practical significance and its relevance for future large-scale quantum processors.

Results

Characterization of power-line noise

Amplitude measurement using echo-based Ramsey spectroscopy

We first benchmark motional coherence using Ramsey spectroscopy on the blue-sideband transition, starting from the qubit ground state and near the motional ground state, which is directly sensitive to secular-frequency fluctuations (see Supplementary Fig. S1 online for experimental details). The Ramsey signal as a function of the evolution time τ exhibits a Gaussian envelope over the first few milliseconds, $C(\tau) \propto \exp[-(\tau/T_g)^2]$, with a characteristic timescale T_g associated with slow frequency fluctuations. Such a non-exponential decay is characteristic of dephasing dominated by slowly varying frequency fluctuations, whereas fast Markovian (Lindblad-type) dephasing leads to an exponential envelope^{14,16}. We therefore infer that Markovian dephasing is subdominant on the timescales probed here, and that the remaining decoherence is dominated by low-frequency contributions such as coherent periodic modulation and slow drift. To suppress slow frequency wander on timescales of $\gtrsim 100$ ms while preserving sensitivity to coherent periodic modulation, we employ an echo-type Ramsey sequence³⁷ (a single π pulse at $\tau/2$) and multi-pulse Carr–Purcell (CP) sequences³⁸ with evenly spaced π pulses. Varying the number of π pulses cross-validates the coherent-modulation signatures across different echo/CP orders while further suppressing slow drift.

In the presence of a sinusoidal modulation of the motional-mode secular frequency, the instantaneous mode frequency becomes $\omega(t) = \omega_0 + \delta\omega(t)$ with $\delta\omega(t) = A \cos(\omega_m t + \phi)$. Here A is the modulation amplitude (in rad/s, equivalently $A/2\pi$ in Hz), $\omega_m = 2\pi f_m$ is the modulation angular frequency, and ϕ is the modulation phase; for power-line-related perturbations one typically has $f_m \approx 50/60$ Hz. This time-dependent secular-frequency shift periodically modulates the phase accumulated during free evolution (i.e., the azimuthal phase of the Bloch vector on the equator), giving rise to revival features in the measured Ramsey signal as a function of the total evolution time τ . In our data, spin-echo Ramsey exhibits revivals at $1/30$ s and its integer multiples, while multi-pulse CP sequences show revivals only at specific fractions such as $1/15$ s and $1/10$ s.

We characterize the periodic modulation of a radial motional mode using CP sequences with $n = 1, 2, 3$ refocusing π pulses ($n = 1$ corresponding to echo Ramsey). The experiment is not synchronized to the 60-Hz power-line signal, so the measured Ramsey signals correspond to phase-averaged results. In the sinusoidal-modulation model, the signal C_n for each n can be calculated analytically as (see Supplementary Information, Sec. 2 for the derivation)

$$C_1(\tau) = J_0\left(\frac{A}{\omega_m} \cdot 4 \sin^2\left(\frac{\omega_m \tau}{4}\right)\right) \quad (1)$$

$$C_2(\tau) = J_0\left(\frac{A}{\omega_m} \cdot 8 \sin^2\left(\frac{\omega_m \tau}{8}\right) \sin\left(\frac{\omega_m \tau}{4}\right)\right) \quad (2)$$

$$C_3(\tau) = J_0\left(\frac{A}{\omega_m} \cdot 4 \sin^2\left(\frac{\omega_m \tau}{12}\right) \left(2 \cos\left(\frac{\omega_m \tau}{3}\right) - 1\right)\right), \quad (3)$$

where J_0 is the Bessel function of the first kind of order zero, and τ is the total free-evolution time (sum of free-evolution intervals), excluding the finite durations of the $\pi/2$ and intermediate π pulses. Fitting these expressions to the data, including a motional-heating envelope, yields $A/2\pi = 40\text{--}54$ Hz and a heating rate $\dot{n} = 6\text{--}14$ for a radial mode with $\omega_0/2\pi \simeq 1.27$ MHz. While the analysis here focuses on coherent sinusoidal modulation, motional heating also contributes to the overall contrast decay. The consideration of heating effects and their interplay with sinusoidal noise is described in detail in the Supplementary Information, Sec. 3, where we use the Quantum Toolbox in Python (QuTiP)³⁹.

Figure 1 shows the measured Ramsey signal as a function of the evolution time τ for $n = 1, 2, 3$, together with fits of the model above to the data. The revivals occur at evolution times set by the 60-Hz line cycle (e.g., for echo Ramsey at integer multiples of $1/30$ s), consistent with a coherent line-synchronous perturbation.

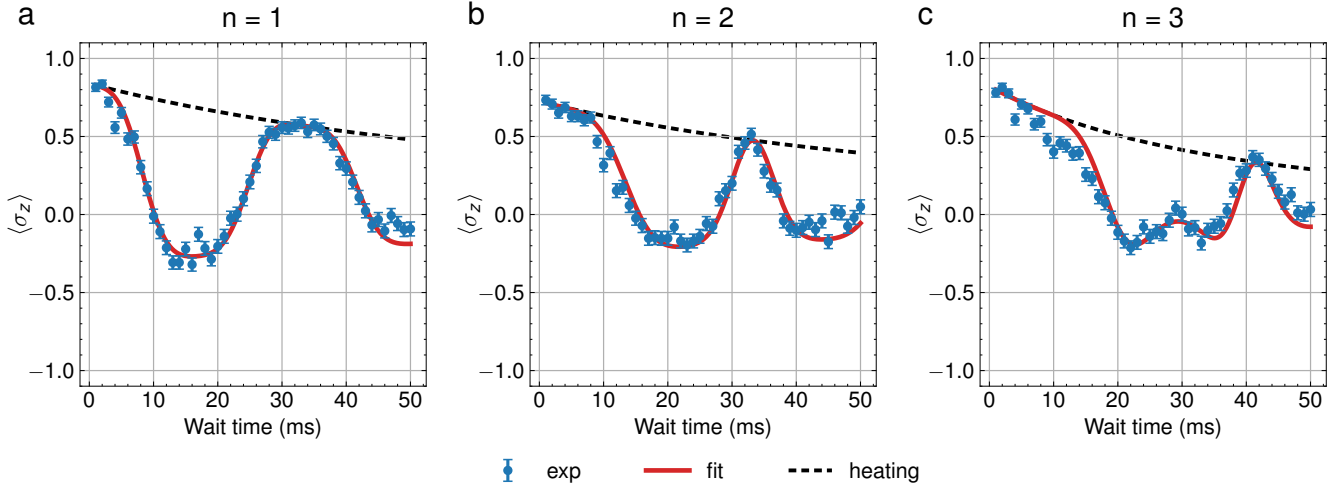


Figure 1. Amplitude characterization of sinusoidal secular-frequency modulation in a radial motional mode using CP sequences with (a) $n = 1$ (echo Ramsey), (b) $n = 2$, and (c) $n = 3$ refocusing pulses. Blue circles show the measured Ramsey signal $\langle \sigma_z \rangle$ with error bars indicating shot noise ($N = 500$ shots per point). Solid red curves show fits to the analytic sinusoidal-modulation model [Eqs. (1)–(3)] including heating effects. Best-fit parameters are (a) $A/2\pi = 53.9(11)$ Hz, $\dot{n} = 6.4(8)$ s $^{-1}$; (b) $A/2\pi = 40.4(12)$ Hz, $\dot{n} = 7.1(15)$ s $^{-1}$; (c) $A/2\pi = 45.5(17)$ Hz, $\dot{n} = 13.6(26)$ s $^{-1}$. Dashed black curves show the independently simulated heating envelope alone; see Supplementary Information, Sec. 3 for simulation details. Revivals occur at evolution times set by the 60-Hz line cycle: for echo Ramsey at integer multiples of 1/30s, and for multi-pulse CP at characteristic fractions (e.g., 1/15s and 1/10s), as predicted by the corresponding $C_n(\tau)$ expressions.

Phase measurement using delay-swept spin-echo Ramsey spectroscopy

In this experiment, we operate in a phase-sensitive mode by synchronizing the start of each experimental shot to a fixed phase of the 60-Hz power-line signal. We then introduce a programmable delay t_d before the pulse sequence, so that the spin-echo Ramsey sequence is executed at a controllable phase of the line cycle (see Supplementary Fig. S1 online for experimental details). Modeling the resulting secular-frequency shift as $\delta\omega(t) = A \cos(\omega_m t + \phi_d)$, the delay deterministically maps to the modulation phase as $\phi_d = \phi_0 + \omega_m t_d$, where ϕ_0 is the modulation phase at zero delay. For each delay (i.e., modulation-phase) setting, we perform a spin-echo Ramsey measurement and fit the analytic expression

$$C(\tau) = \cos(\varphi(\tau)), \quad \varphi(\tau) = \int_0^{\tau/2} A \cos(\omega_m t + \phi_d) dt - \int_{\tau/2}^{\tau} A \cos(\omega_m t + \phi_d) dt \quad (4)$$

to the measured Ramsey signal to extract the modulation phase ϕ_d for that delay. Here $\varphi(\tau)$ is the phase accumulated during the echo sequence due to the sinusoidal secular-frequency shift.

We find that the two radial modes (X and Y) exhibit different modulation amplitude A while sharing essentially the same modulation phase ϕ_d as a function of the delay relative to the power-line trigger. This in-phase behavior suggests that the 60-Hz perturbation couples through the trap RF drive, producing a common-mode secular-frequency modulation in both modes. Figure 2a shows the delay-dependent spin-echo Ramsey fringes, while Fig. 2b compares the extracted phases for the two modes.

Verification via spin-echo Ramsey tracking

We verify the above characterization of the 60-Hz power-line noise by implementing a spin-echo Ramsey sequence in which the predicted phase accumulation during the free-evolution time is compensated. Using the estimated power-line phase extracted from the delay-swept measurements in Fig. 2, we calculate the expected phase accumulation during the free-evolution interval of the spin-echo Ramsey sequence. This predicted phase is then applied to the phase of the second $\pi/2$ pulse, thereby passively compensating the phase shift induced by the 60-Hz modulation. As shown by the orange diamond points in Fig. 2a, applying this post-phase correction largely eliminates the dependence on the power-line noise, indicating that the extracted noise parameters capture the dominant contribution to the observed secular-frequency modulation.

Cancellation of 60-Hz power-line noise

To actively cancel the 60-Hz power-line noise, we inject a sinusoidal compensation signal at the power-line frequency into the set point of the Proportional-Integral (PI) controller, as described in Methods. When the compensation signal has the same

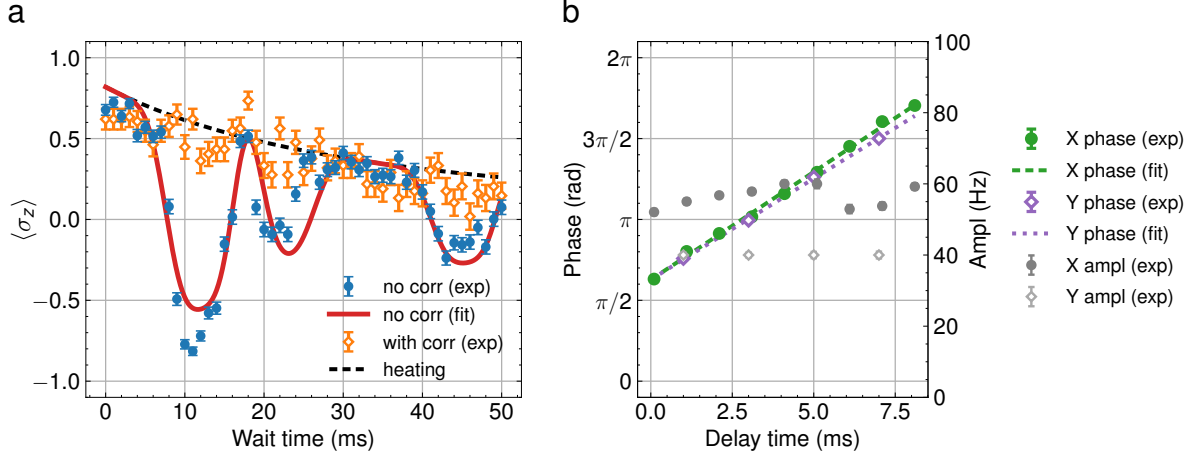


Figure 2. Phase characterization of sinusoidal secular-frequency modulation in radial motional modes using delay-swept spin-echo Ramsey measurements. (a) Delay-swept spin-echo Ramsey measurement at a representative trigger delay of 2 ms. The data are plotted in the same format as in Fig. 1: the experiment (blue circles with error bars indicating shot noise, $N = 500$ shots per point), a fit including sinusoidal noise and heating effects (solid red curve), and the heating effects alone (dashed black curve). Best-fit parameters are $A/2\pi = 56.8(7)$ Hz, $\phi_d = 0.913(3)\pi$, and $\dot{n} = 15.5(8) \text{ s}^{-1}$. Orange diamonds show the passive phase-correction verification with error bars indicating shot noise ($N = 150$ shots per point); see *Verification via spin-echo Ramsey tracking*. (b) Extracted modulation amplitude (dark-gray circle and bright-gray diamonds for the X and Y modes, respectively) and phase (green circle and purple diamonds for the X and Y modes, respectively) for the two radial modes as a function of the delay relative to the power-line trigger. The fitted phase-evolution slopes (dashed green and dotted purple curves for the X and Y modes, respectively) are $2\pi \times 66.7(3) \text{ s}^{-1}$ for the X mode and $2\pi \times 62.5(9) \text{ s}^{-1}$ for the Y mode, both of which are close to the expected value of $2\pi \times 60 \text{ s}^{-1}$, confirming that the modulation is synchronous with the 60-Hz power-line signal.

amplitude but an opposite phase relative to the ambient 60-Hz noise, the resulting periodic secular-frequency modulation is canceled.

The amplitude of the 60-Hz component is first estimated from the characterization results above. However, the phase of the compensation signal cannot be determined directly, because the injected 60-Hz tone is not phase-referenced to the experimental trigger; consequently, the relative phase between the injected tone and the ambient 60-Hz perturbation is unknown a priori. To overcome this, we perform a phasor-fitting procedure in which compensation signals with various amplitudes (V_i) and phases (\hat{u}_i) are sequentially injected into the controller. Here \hat{u}_i denotes a unit phasor ($|\hat{u}_i| = 1$) specifying the injected phase in the 60-Hz phasor plane. For each trial signal, the residual 60-Hz modulation amplitude (A_i) is measured using spin-echo Ramsey sequences. The relationship between the injected signal and the measured residual amplitude is then used to extract the optimal amplitude (V) and phase (\hat{u}) of the compensation signal by minimizing

$$\arg \min_{V, \hat{u}, r} \sum_i [|V\hat{u} - V_i\hat{u}_i| - rA_i]^2. \quad (5)$$

Here r is a proportionality constant that converts the measured modulation amplitude A_i (in frequency units) to the corresponding phasor magnitude (in voltage units), accounting for the unknown transfer gain between the injected set-point modulation and the resulting secular-frequency modulation. This optimization yields a vector representation of the 60-Hz noise phasor, allowing us to directly determine the opposite-phase compensation signal required for cancellation. Figure 3a shows the phasor plot of the injected compensation signals and the corresponding residual amplitudes, from which the noise phasor is extracted. Applying the resulting opposite-phase signal substantially suppresses the 60-Hz modulation in the spin-echo Ramsey measurements [Fig. 3b], demonstrating effective reduction of the dominant periodic noise component. As a result, the coherence time of the radial motional mode increases from approximately 10 ms to 35 ms, close to the limit expected from the heating rate ($\dot{n} = 15 \text{ s}^{-1}$). Notably, once optimized, the same compensation settings continued to suppress the 60-Hz component over at least one month, highlighting the suitability of the method for long-term operation.

Discussion

The present active cancellation scheme, which relies on a PI controller and an externally generated 60-Hz compensation signal, effectively suppresses the dominant power-line noise in our system. However, the implementation could be simplified and made

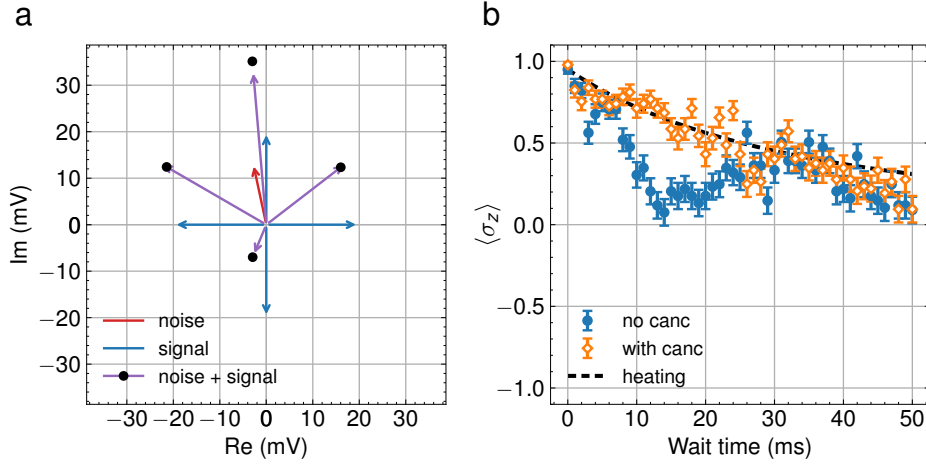


Figure 3. Active cancellation of sinusoidal secular-frequency modulation using phasor-based optimization. (a) Phasor diagram used for the least-squares optimization of the 60-Hz compensation signal. Blue arrows denote the injected compensation phasors $V_i \hat{u}_i$ for four trial settings. The red arrow indicates the extracted 60-Hz noise phasor $-V \hat{u}$. The extracted noise phasor has amplitude $V = 14(3)$ mV and phase $\arg(-\hat{u}) = 102(10)^\circ$, and the scale factor is $r = 0.38(4)$ mV/Hz. Purple arrows show the resulting residual phasors $V_i \hat{u}_i - V \hat{u}$; black dots mark their endpoints, whose amplitudes are proportional to the measured residual modulation amplitude A_i (after applying the scale factor r defined in the text). (b) Echo-Ramsey signal of a radial motional mode with and without active cancellation. Blue circles and orange diamonds show the data without and with cancellation applied, respectively, with error bars indicating shot noise ($N = 150$ shots per point) for both datasets; the dashed black curve shows the independently simulated heating envelope (using an average heating rate $\dot{n} = 15$ s $^{-1}$). Active cancellation suppresses the 60-Hz modulation and extends the coherence time from ~ 10 ms to ~ 35 ms, close to the heating-limited value.

more efficient. Rather than using a dedicated signal generator, a 60-Hz reference could be derived directly from the power line using an electrically isolated sensing stage, followed by a controllable phase shift and amplitude scaling before injection into the controller set-point. Alternatively, the power-line reference could be digitized with an ADC and processed in real time (e.g., with a programmable phase and gain), and the resulting compensation waveform could be synthesized with a DAC for injection into the set-point. Such an approach would reduce hardware complexity while preserving tunable amplitude and phase control for optimal cancellation.

The physical origin of the 60-Hz perturbation is likely multifaceted. In our setup, several essential devices—such as control electronics, RF amplifiers, and vacuum system components—must remain continuously connected to the power line. Together with possible ground loops and electromagnetic pickup in the laboratory wiring, these connections can provide pathways for periodic interference to couple into the ion-trap electronics and modulate the effective confinement.

Even after the active cancellation of the 60-Hz component, residual fluctuations persist in the motional-mode secular frequencies. In our measurements, the remaining noise is well described by a slow stochastic frequency drift with a characteristic scale on the order of tens of hertz (see Supplementary Information, Sec. 4). Because this residual drift is not phase-referenced to the power line, it is not addressed by the present feedforward scheme. Identifying the dominant mechanism and implementing complementary stabilization beyond power-line-synchronous feedforward remain important directions for future work.

Methods

Experimental setup

We trap a single $^{171}\text{Yb}^+$ ion in a blade-type linear Paul trap, as described in our previous work^{40,41}. The secular frequencies are $\omega_{x,y,z} \simeq 2\pi \times (910, 1270, 120)$ kHz; the axial mode at 120 kHz is not used in this study. The qubit is encoded in the hyperfine clock states $|\downarrow\rangle = |S_{1/2}, F=0, m_F=0\rangle$ and $|\uparrow\rangle = |S_{1/2}, F=1, m_F=0\rangle$. State initialization and readout are performed using standard optical pumping and state-dependent fluorescence detection via the cycling transition, from which the population in $|\uparrow\rangle$ is inferred⁴². We prepare the relevant motional modes close to their ground states using resolved sideband cooling prior to each experiment. The Raman beams used for spin-motion coupling are aligned such that the wavevector difference $\Delta\mathbf{k}$ is perpendicular to the trap axis, thereby coupling predominantly to the radial motional modes⁴¹.

RF system and PI controller

The ion trap is driven by an RF source at approximately 17 MHz and applied to the trap electrodes via a helical resonator. The RF-drive amplitude is stabilized using a PI servo loop (New Focus LB1005 High-Speed Servo Controller), which adjusts the RF amplitude so that the measured amplitude tracks a set-point input; changes in the RF amplitude correspondingly shift the trap secular frequencies⁴³. To enable active cancellation of periodic noise, a periodic compensation signal is added to the set-point input of the PI controller, as illustrated schematically in Fig. 4.

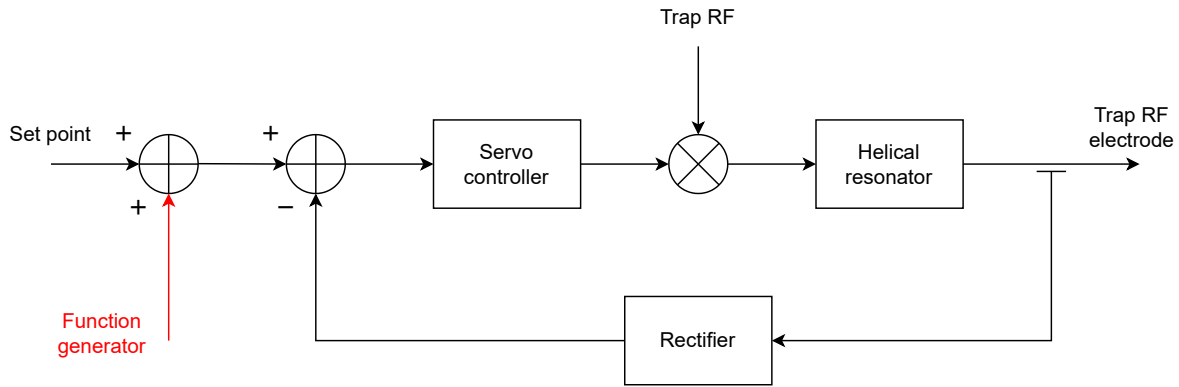


Figure 4. Schematic of the RF stabilization and compensation circuit. The set-point is combined with an externally injected compensation tone, and the resulting reference is compared with a rectified monitor signal derived from the trap RF output. The error signal drives a servo that controls the RF-drive amplitude via amplitude modulation of the RF source. After filtering by the helical resonator, the RF is delivered to the trap electrodes, and a fraction of the RF is fed back for rectification and stabilization.

Active cancellation implementation

The compensation-signal amplitude is initially estimated relative to the PI controller set-point. In our configuration, maintaining a secular frequency of approximately 1 MHz requires a set-point voltage of about 1.43 V. Assuming a locally linear response between the set-point and the secular frequency, an unwanted 60-Hz modulation with an effective magnitude of ~ 50 Hz corresponds to a set-point modulation on the order of $\sim 70 \mu\text{V}$. To generate a compensation signal at this level, we use a commercial signal generator in combination with fixed attenuation, adjusting the generator output amplitude such that a modulation on the order of tens of μV is applied at the set-point input.

In practice, the power-line frequency is not perfectly constant at 60 Hz and can drift by up to $\sim \pm 1$ Hz over the course of an experiment. Direct injection of a continuous 60-Hz tone would therefore lead to gradual phase slips between the compensation signal and the ambient perturbation, reducing cancellation efficiency. To address this, we employ the burst mode of the signal generator, following a previously reported approach³⁵. Using a trigger derived from the power line, the generator outputs a single-cycle sinusoidal burst at 62 Hz, i.e., one cycle at a slightly higher frequency than the nominal 60 Hz. This ensures that the output waveform terminates before the next trigger event, allowing the phase to be re-referenced on every cycle and preventing accumulation of phase error.

Data availability

The datasets generated during and/or analysed during the current study are available from the corresponding author on reasonable request.

References

1. Cirac, J. I. & Zoller, P. Quantum computations with cold trapped ions. *Phys. Rev. Lett.* **74**, 4091–4094, DOI: <https://doi.org/10.1103/PhysRevLett.74.4091> (1995).
2. Sørensen, A. & Mølmer, K. Quantum computation with ions in thermal motion. *Phys. Rev. Lett.* **82**, 1971–1974, DOI: <https://doi.org/10.1103/PhysRevLett.82.1971> (1999).
3. Mintert, F. & Wunderlich, C. Ion-trap quantum logic using long-wavelength radiation. *Phys. Rev. Lett.* **87**, 257904, DOI: <https://doi.org/10.1103/PhysRevLett.87.257904> (2001).

4. Leibfried, D. *et al.* Experimental demonstration of a robust, high-fidelity geometric two ion-qubit phase gate. *Nature* **422**, 412–415, DOI: <https://doi.org/10.1038/nature01492> (2003).
5. Leibfried, D., Blatt, R., Monroe, C. & Wineland, D. Quantum dynamics of single trapped ions. *Rev. Mod. Phys.* **75**, 281–324, DOI: <https://doi.org/10.1103/RevModPhys.75.281> (2003).
6. Bruzewicz, C. D., Chiaverini, J., McConnell, R. & Sage, J. M. Trapped-ion quantum computing: progress and challenges. *Appl. Phys. Rev.* **6**, 021314, DOI: <https://doi.org/10.1063/1.5088164> (2019).
7. Katz, O., Feng, L., Risinger, A., Monroe, C. & Cetina, M. Demonstration of three- and four-body interactions between trapped-ion spins. *Nat. Phys.* **19**, 1452–1458, DOI: <https://doi.org/10.1038/s41567-023-02102-7> (2023).
8. Flühmann, C. *et al.* Encoding a qubit in a trapped-ion mechanical oscillator. *Nature* **566**, 513–517, DOI: <https://doi.org/10.1038/s41586-019-0960-6> (2019).
9. Matsos, V. G. *et al.* Universal quantum gate set for Gottesman–Kitaev–Preskill logical qubits. *Nat. Phys.* **21**, 1664–1669, DOI: <https://doi.org/10.1038/s41567-025-03002-8> (2025).
10. Soare, A. *et al.* Experimental noise filtering by quantum control. *Nat. Phys.* **10**, 825–829, DOI: <https://doi.org/10.1038/nphys3115> (2014).
11. Green, T. J. & Biercuk, M. J. Phase-modulated decoupling and error suppression in qubit-oscillator systems. *Phys. Rev. Lett.* **114**, 120502, DOI: <https://doi.org/10.1103/PhysRevLett.114.120502> (2015).
12. Bermudez, A. *et al.* Assessing the progress of trapped-ion processors towards fault-tolerant quantum computation. *Phys. Rev. X* **7**, 041061, DOI: <https://doi.org/10.1103/PhysRevX.7.041061> (2017).
13. Milne, A. R. *et al.* Phase-modulated entangling gates robust to static and time-varying errors. *Phys. Rev. Appl.* **13**, 024022, DOI: <https://doi.org/10.1103/PhysRevApplied.13.024022> (2020).
14. Suter, D. & Álvarez, G. A. Colloquium: Protecting quantum information against environmental noise. *Rev. Mod. Phys.* **88**, 041001, DOI: <https://doi.org/10.1103/RevModPhys.88.041001> (2016).
15. Álvarez, G. A. & Suter, D. Measuring the spectrum of colored noise by dynamical decoupling. *Phys. Rev. Lett.* **107**, 230501, DOI: <https://doi.org/10.1103/PhysRevLett.107.230501> (2011).
16. Ithier, G. *et al.* Decoherence in a superconducting quantum bit circuit. *Phys. Rev. B* **72**, 134519, DOI: <https://doi.org/10.1103/PhysRevB.72.134519> (2005).
17. Bylander, J. *et al.* Noise spectroscopy through dynamical decoupling with a superconducting flux qubit. *Nat. Phys.* **7**, 565–570, DOI: <https://doi.org/10.1038/nphys1994> (2011).
18. Romach, Y. *et al.* Spectroscopy of surface-induced noise using shallow spins in diamond. *Phys. Rev. Lett.* **114**, 017601, DOI: <https://doi.org/10.1103/PhysRevLett.114.017601> (2015).
19. Connors, E. J., Nelson, J., Edge, L. F. & Nichol, J. M. Charge-noise spectroscopy of Si/SiGe quantum dots via dynamically-decoupled exchange oscillations. *Nat. Commun.* **13**, 940, DOI: <https://doi.org/10.1038/s41467-022-28519-x> (2022).
20. McCormick, K. C., Keller, J., Wineland, D. J., Wilson, A. C. & Leibfried, D. Coherently displaced oscillator quantum states of a single trapped atom. *Quantum Sci. Technol.* **4**, 024010, DOI: <https://doi.org/10.1088/2058-9565/ab0513> (2019).
21. Milne, A. R. *et al.* Quantum oscillator noise spectroscopy via displaced cat states. *Phys. Rev. Lett.* **126**, 250506, DOI: <https://doi.org/10.1103/PhysRevLett.126.250506> (2021).
22. Keller, J. *et al.* Quantum harmonic oscillator spectrum analyzers. *Phys. Rev. Lett.* **126**, 250507, DOI: <https://doi.org/10.1103/PhysRevLett.126.250507> (2021).
23. Cai, M.-L. *et al.* Observation of a quantum phase transition in the quantum Rabi model with a single trapped ion. *Nat. Commun.* **12**, 1126, DOI: <https://doi.org/10.1038/s41467-021-21425-8> (2021).
24. de Neeve, B., Nguyen, T.-L., Behrle, T. & Home, J. P. Error correction of a logical grid state qubit by dissipative pumping. *Nat. Phys.* **18**, 296–300, DOI: <https://doi.org/10.1038/s41567-021-01487-7> (2022).
25. Vepsäläinen, A. *et al.* Improving qubit coherence using closed-loop feedback. *Nat. Commun.* **13**, 1932, DOI: <https://doi.org/10.1038/s41467-022-29287-4> (2022).
26. Masuyama, Y. *et al.* Gradiometer using separated diamond quantum magnetometers. *Sensors* **21**, 0977, DOI: <https://doi.org/10.3390/s21030977> (2021).
27. Tayefeh Younesi, A., Omar, M., Wickenbrock, A., Budker, D. & Ulbricht, R. Towards high-sensitivity magnetometry with nitrogen-vacancy centers in diamond using the singlet infrared absorption. *Phys. Rev. Appl.* **23**, 054019, DOI: <https://doi.org/10.1103/PhysRevApplied.23.054019> (2025).

28. Bharadwaj, R. *et al.* Active noise reduction in gated quantum devices. *Appl. Phys. Lett.* **127**, 264002, DOI: <https://doi.org/10.1063/5.0303853> (2025).
29. Schindler, P. *et al.* A quantum information processor with trapped ions. *New J. Phys.* **15**, 123012, DOI: <https://doi.org/10.1088/1367-2630/15/12/123012> (2013).
30. Zhang, J. *et al.* Discrimination and estimation for dephasing sources of trapped ion qubits. *Appl. Phys. B* **126**, 20, DOI: <https://doi.org/10.1007/s00340-019-7366-x> (2020).
31. Wang, P. *et al.* Single ion qubit with estimated coherence time exceeding one hour. *Nat. Commun.* **12**, 233, DOI: <https://doi.org/10.1038/s41467-020-20330-w> (2021).
32. Kranzl, F. *et al.* Controlling long ion strings for quantum simulation and precision measurements. *Phys. Rev. A* **105**, 052426, DOI: <https://doi.org/10.1103/PhysRevA.105.052426> (2022).
33. Gan, H. C. J. *Continuous variables quantum information processing with trapped ions*. Ph.D. thesis, National University of Singapore (2019).
34. Merkel, B. *et al.* Magnetic field stabilization system for atomic physics experiments. *Rev. Sci. Instrum.* **90**, 044702, DOI: <https://doi.org/10.1063/1.5080093> (2019).
35. Hu, H. *et al.* Compensation of power line-induced magnetic interference in trapped-ion system. *Appl. Phys. B* **129**, 163, DOI: <https://doi.org/10.1007/s00340-023-08106-8> (2023).
36. Flühmann, C. *Encoding a qubit in the motion of a trapped ion using superpositions of displaced squeezed states*. Ph.D. thesis, ETH Zurich (2019). DOI: <https://doi.org/10.3929/ethz-b-000355836>.
37. Hahn, E. L. Spin echoes. *Phys. Rev.* **80**, 580–594, DOI: <https://doi.org/10.1103/PhysRev.80.580> (1950).
38. Carr, H. Y. & Purcell, E. M. Effects of diffusion on free precession in nuclear magnetic resonance experiments. *Phys. Rev.* **94**, 630–638, DOI: <https://doi.org/10.1103/PhysRev.94.630> (1954).
39. Johansson, J. R., Nation, P. D. & Nori, F. QuTiP 2: a Python framework for the dynamics of open quantum systems. *Comput. Phys. Commun.* **184**, 1234–1240, DOI: <https://doi.org/10.1016/j.cpc.2012.11.019> (2013).
40. Jeon, H. *et al.* Experimental realization of entangled coherent states in two-dimensional harmonic oscillators of a trapped ion. *Sci. Rep.* **14**, 6847, DOI: <https://doi.org/10.1038/s41598-024-57391-6> (2024).
41. Jeon, H. *et al.* Two-mode bosonic state tomography with single-shot joint-parity measurement of a trapped ion. *PRX Quantum* **6**, 040352, DOI: <https://doi.org/10.1103/wsqr-j9f4> (2025).
42. Olmschenk, S. *et al.* Manipulation and detection of a trapped Yb⁺ hyperfine qubit. *Phys. Rev. A* **76**, 052314, DOI: <https://doi.org/10.1103/PhysRevA.76.052314> (2007).
43. Park, Y. *et al.* A new measurement method for high voltages applied to an ion trap generated by an RF resonator. *Sensors* **21**, 1143, DOI: <https://doi.org/10.3390/s21041143> (2021).

Acknowledgements

This work was supported by the National Research Foundation of Korea (NRF) grant (No. RS-2024-00442855, No. RS-2024-00413957) and the Institute for Information & Communications Technology Planning & Evaluation (IITP) grant (No.RS-2022-II221040), all funded by the Korean government (MSIT).

Author contributions statement

J.Y. designed, carried out, and analyzed the experiments. J.K. provided experimental guidance, particularly on the setup and control system. J.Y., J.K., K.K., and W.C. contributed to the construction of the experimental apparatus. T.K. supervised the project. All authors reviewed and discussed the experimental results and contributed to the manuscript.

Competing interests

The authors declare no competing interests.

Supplementary Information

Characterization and active cancellation of power-line-induced motional-mode frequency noise in a trapped-ion system

Jaehun You^{1,2,3}, Jiyong Kang^{1,2,3}, Kyunghye Kim^{1,2,3}, Wonhyeong Choi^{1,2,3}, and Taehyun Kim^{1,2,3,4,5,*}

¹Department of Computer Science and Engineering, Seoul National University, Seoul, 08826, Republic of Korea

²Automation and Systems Research Institute, Seoul National University, Seoul, 08826, Republic of Korea

³NextQuantum, Seoul National University, Seoul, 08826, Republic of Korea

⁴Institute of Computer Technology, Seoul National University, Seoul, 08826, Republic of Korea

⁵Institute of Applied Physics, Seoul National University, Seoul, 08826, Republic of Korea

1 Experimental sequence

Figure S1 illustrates the experimental sequence for the case of a single refocusing pulse ($n = 1$), i.e., the *echo Ramsey* sequence. After qubit initialization and resolved sideband cooling, the system is prepared in $|\psi_s\rangle|\psi_m\rangle = |\downarrow\rangle|0\rangle$, where the subscripts s and m denote the spin qubit and the motional mode, respectively. A $\pi/2$ pulse on the blue-sideband transition then creates a coherent superposition between $|\downarrow\rangle|0\rangle$ and $|\uparrow\rangle|1\rangle$. The system is then allowed to evolve for a total time τ with a refocusing π pulse at $\tau/2$, and finally analyzed with a second $\pi/2$ pulse followed by state-dependent fluorescence detection.

For the *amplitude characterization* measurements, we do not employ the trigger-delay block; each shot proceeds directly from initialization to the echo-Ramsey sequence.

For the *phase characterization* measurements, as indicated by the dashed box in Fig. S1, we additionally synchronize the start of each experimental shot to a fixed phase of the 60-Hz power-line signal and insert a programmable delay time t_d before the pulse sequence.

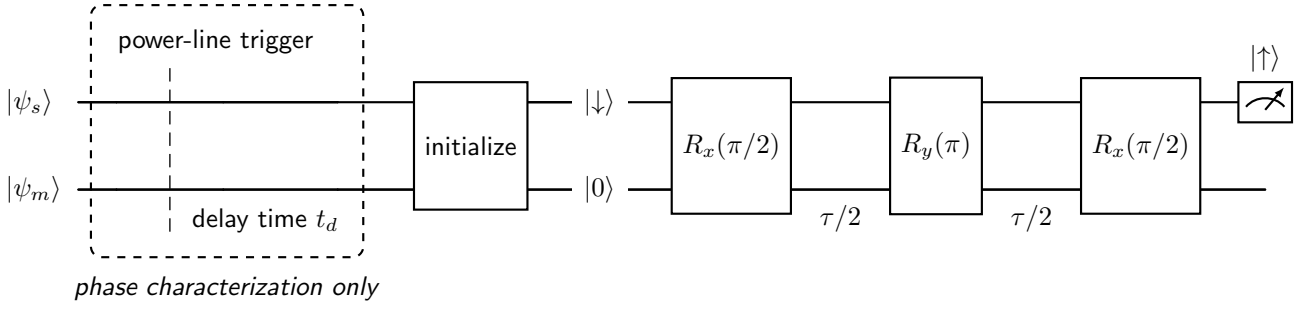


Figure S1: Experimental timing diagram for the full sequence (shown for the echo-Ramsey case with $n = 1$). Here $|\psi_s\rangle$ and $|\psi_m\rangle$ denote the spin-qubit and motional-mode states, respectively, and each shot is initialized to $|\psi_s\rangle|\psi_m\rangle = |\downarrow\rangle|0\rangle$ by qubit initialization and resolved sideband cooling. The echo-Ramsey sequence is implemented on the blue-sideband transition between $|\downarrow\rangle|0\rangle$ and $|\uparrow\rangle|1\rangle$, with a single refocusing π pulse at $\tau/2$. The dashed box indicates the optional 60-Hz power-line trigger and programmable delay t_d used only for phase characterization; it is omitted for amplitude characterization.

2 Echo-based Ramsey signal under sinusoidal secular-frequency modulation

Model and definition. We model the motional-mode secular-frequency shift as a sinusoidal modulation,

$$\delta\omega(t) = A \cos(\omega_m t + \phi),$$

with modulation amplitude A and angular frequency ω_m . The initial phase ϕ is assumed to be uniformly distributed on $[0, 2\pi)$. We consider a Carr–Purcell (CP) sequence with n refocusing π pulses and define the toggling function $y_n(t) \in \{+1, -1\}$, which flips sign at each π pulse^{1,2}. The accumulated phase after total evolution time τ is

$$\varphi_n(\tau) = \int_0^\tau y_n(t) \delta\omega(t) dt.$$

The phase-averaged Ramsey signal is given by

$$C_n(\tau) = \langle \cos(\varphi_n(\tau)) \rangle_\phi.$$

Using the identity $J_0(z) = \frac{1}{2\pi} \int_0^{2\pi} \cos(z \sin(\phi)) d\phi$, we obtain

$$C_n(\tau) = J_0\left(\frac{A}{\omega_m} F_n(\omega_m \tau)\right),$$

where F_n is a dimensionless function determined by the pulse pattern.

Ramsey ($n = 0$). With no refocusing pulse, $y_0(t) = +1$ on $[0, \tau]$.

$$\begin{aligned} \varphi_0(\tau) &= A \int_0^\tau \cos(\omega_m t + \phi) dt = \frac{A}{\omega_m} \cdot 2 \sin\left(\frac{\omega_m}{2} \tau\right) \cos\left(\frac{\omega_m}{2} \tau + \phi\right) \\ C_0(\tau) &= \frac{1}{2\pi} \int_0^{2\pi} \cos\left[\frac{A}{\omega_m} \cdot 2 \sin\left(\frac{\omega_m}{2} \tau\right) \cos\left(\frac{\omega_m}{2} \tau + \phi\right)\right] d\phi \\ &= J_0\left(\frac{A}{\omega_m} \cdot 2 \sin\left(\frac{\omega_m}{2} \tau\right)\right), \end{aligned}$$

which yields $F_0(\vartheta) = 2 \sin(\vartheta/2)$.

Echo-based Ramsey ($n = 1, 2, 3$).

(a) Echo Ramsey, $n = 1$: The π pulse is applied at $t = \tau/2$, so that $y_1(t) = +1, -1$ on the two segments.

$$\begin{aligned}\varphi_1(\tau) &= A \left[\int_0^{\tau/2} \cos(\omega_m t + \phi) dt - \int_{\tau/2}^{\tau} \cos(\omega_m t + \phi) dt \right] \\ &= \frac{A}{\omega_m} \cdot 4 \sin^2\left(\frac{\omega_m \tau}{4}\right) \sin\left(\frac{\omega_m \tau}{2} + \phi\right) \\ C_1(\tau) &= J_0\left(\frac{A}{\omega_m} \cdot 4 \sin^2\left(\frac{\omega_m \tau}{4}\right)\right),\end{aligned}$$

which yields $F_1(\vartheta) = 4 \sin^2(\vartheta/4)$.

(b) CP with $n = 2$: The π pulses are applied at $t = \tau/4$ and $t = 3\tau/4$, so that $y_2(t) = +1, -1, +1$ on the three segments.

$$\begin{aligned}\varphi_2(\tau) &= A \left[\int_0^{\tau/4} \cos(\omega_m t + \phi) dt - \int_{\tau/4}^{3\tau/4} \cos(\omega_m t + \phi) dt + \int_{3\tau/4}^{\tau} \cos(\omega_m t + \phi) dt \right] \\ &= -\frac{A}{\omega_m} \cdot 8 \sin^2\left(\frac{\omega_m \tau}{8}\right) \sin\left(\frac{\omega_m \tau}{4}\right) \cos\left(\frac{\omega_m \tau}{2} + \phi\right) \\ C_2(\tau) &= J_0\left(\frac{A}{\omega_m} \cdot 8 \sin^2\left(\frac{\omega_m \tau}{8}\right) \sin\left(\frac{\omega_m \tau}{4}\right)\right),\end{aligned}$$

which yields $F_2(\vartheta) = 8 \sin^2(\vartheta/8) \sin(\vartheta/4)$.

(c) CP with $n = 3$: The π pulses are applied at $t = \tau/6$, $t = \tau/2$, and $t = 5\tau/6$, so that $y_3(t) = +1, -1, +1, -1$ on the four segments. Following the same steps as above, we obtain

$$C_3(\tau) = J_0\left(\frac{A}{\omega_m} \cdot 4 \sin^2\left(\frac{\omega_m \tau}{12}\right) \left(2 \cos\left(\frac{\omega_m \tau}{3}\right) - 1\right)\right),$$

which yields $F_3(\vartheta) = 4 \sin^2(\vartheta/12)(2 \cos(\vartheta/3) - 1)$.

Remarks. (i) The Bessel-function dependence arises from averaging over the unknown initial phase ϕ . (ii) The functions F_n are determined by the pulse pattern; for general n , they can be obtained by summing the signed time-domain integrals over each free-evolution segment.

3 Heating effect on echo-based Ramsey signal

We quantify how motional heating modifies the echo-based Ramsey signal by performing full density-matrix simulations. The motional heating is modeled by a Lindblad term that increases the mean phonon number at a rate $\dot{\bar{n}} = 6 \text{ s}^{-1}$. We numerically integrate the corresponding master equation using the Quantum Toolbox in Python (QuTiP)³.

To isolate the role of heating, we first compute a heating envelope $C_{\text{heat}}(\tau)$ by simulating the same sequence with heating included but without sinusoidal secular-frequency modulation. This envelope is shown as the dashed black curve in Fig. S2 and captures the reduction of the Ramsey contrast due solely to heating.

Next, we compute the Ramsey signal in the absence of heating, $C_0(\tau)$ (dotted brown curve), which includes the sinusoidal secular-frequency modulation. Finally, we perform the full simulation including both the secular-frequency modulation and motional heating to obtain $C_{\text{tot}}(\tau)$ (blue points).

As demonstrated in Fig. S2, $C_{\text{tot}}(\tau)$ is well approximated by the product of the heating envelope and the no-heating signal,

$$C_{\text{tot}}(\tau) \approx C_{\text{heat}}(\tau) C_0(\tau),$$

shown as the solid red curve. The near-perfect overlap indicates that, in our parameter regime, heating acts predominantly as a multiplicative amplitude decay and approximately factorizes from the sinusoidal secular-frequency modulation. This factorization allows us to incorporate heating in fits using a separable envelope, while keeping the secular-frequency modulation model unchanged, enabling robust extraction of both the heating rate and modulation parameters.

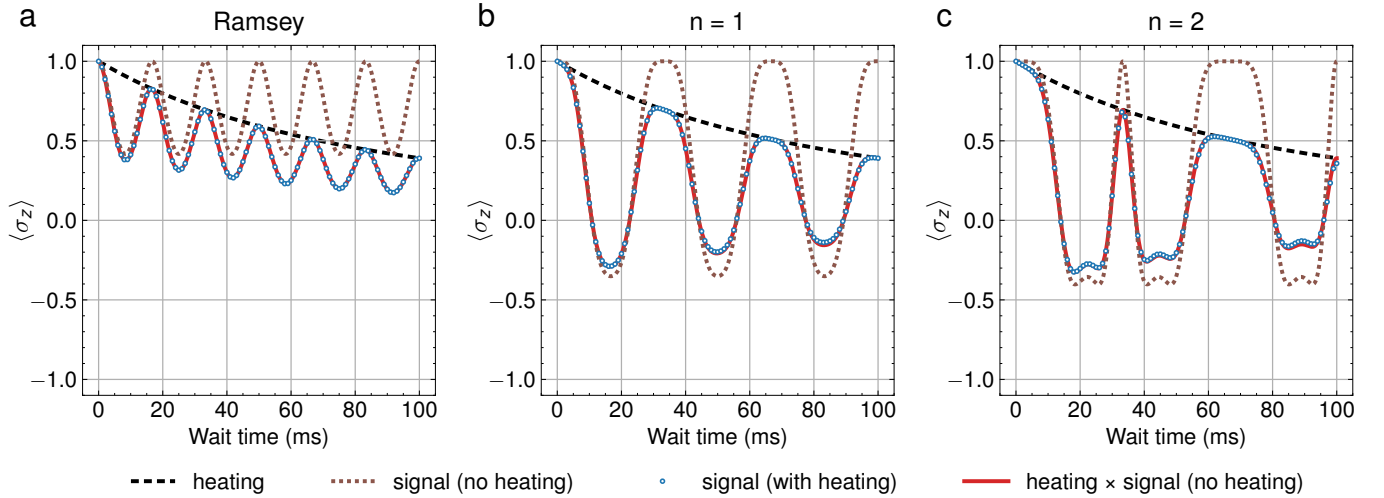


Figure S2: Effect of motional heating on echo-based Ramsey signals. Dashed black curves: heating envelope $C_{\text{heat}}(\tau)$ obtained from a Lindblad heating model with $\dot{\bar{n}} = 6 \text{ s}^{-1}$. Dotted brown curves: simulated Ramsey signals without heating, $C_0(\tau)$, including the sinusoidal secular-frequency modulation. Blue points: full simulations including both the sinusoidal secular-frequency modulation and motional heating, $C_{\text{tot}}(\tau)$. Solid red curves: product model $C_{\text{heat}}(\tau) C_0(\tau)$, showing near-perfect agreement with the full simulation. Panels (a–c) correspond to Ramsey, echo-based Ramsey ($n = 1$), and Carr–Purcell ($n = 2$), respectively.

4 Residual slow frequency drift

Although active cancellation of the 60-Hz power-line noise extends the coherence time inferred from echo-Ramsey measurements to approximately 35 ms, this value does not reflect the practically usable timescale. To probe the residual dephasing, we perform a Ramsey measurement without the refocusing π pulse and quantify the Ramsey contrast as the wait time is varied. Figure S3a shows the resulting contrast decay, together with the independently simulated heating envelope. For each wait-time setting, we scan the phase of the second $\pi/2$ pulse to record a Ramsey fringe [inset of Fig. S3a] and extract the contrast from a sinusoidal fit to the phase-scan data. Despite active cancellation, the contrast exhibits a rapid decay beyond about 5 ms, indicating that additional dephasing processes remain.

To characterize this residual noise, we fix the Ramsey wait time to ~ 2 ms and repeat the measurement continuously over 250 s. Figure S3b shows the resulting single-shot outcomes $P_1(t)$ for the two radial modes, where slow fluctuations reflect drifts of the motional-mode frequency. As shown in the inset, we choose the wait time near $P_1 \approx 0.5$ (around 2 ms), where the Ramsey signal has maximal slope and is therefore most sensitive to small frequency shifts. Assuming the residual noise is slow stochastic frequency drift, the observed Ramsey-signal fluctuations correspond to a standard deviation on the order of tens of hertz in the motional-mode secular frequency. Such slow fluctuations impose a practical limitation on coherence, even when the 60-Hz component is actively suppressed.

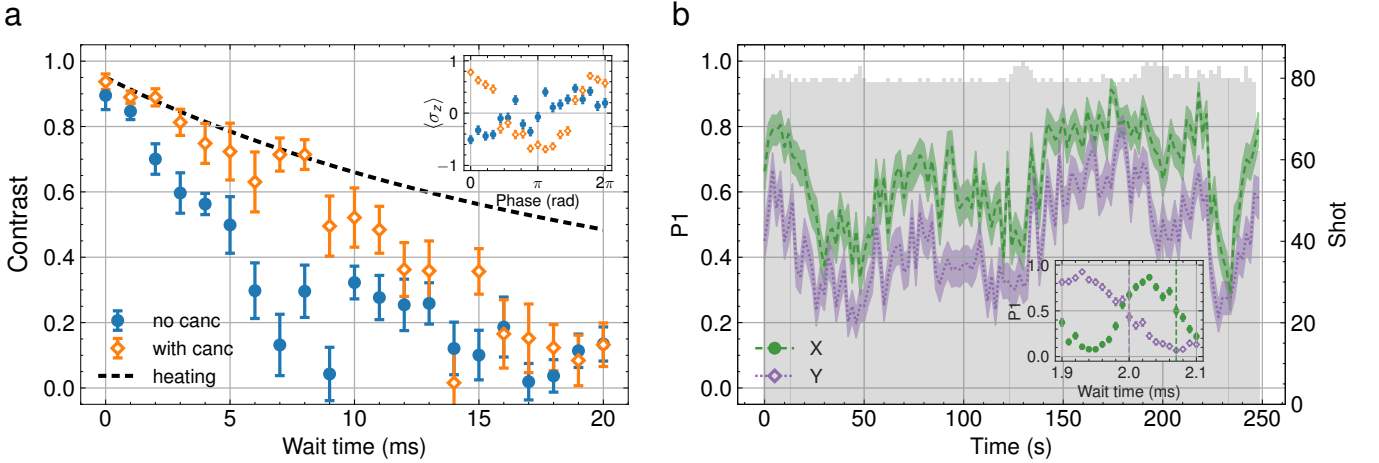


Figure S3: Residual dephasing from slow stochastic drift after active cancellation of the 60-Hz component. (a) Ramsey-contrast decay (no refocusing π pulse) versus wait time for a radial motional mode, measured without cancellation (blue circles) and with active cancellation (orange diamonds). At each wait time, the contrast is extracted from a sinusoidal fit to a phase scan of the second $\pi/2$ pulse (inset). The dashed black curve shows the independently simulated heating envelope. (b) Time trace of single-shot Ramsey outcomes $P_1(t)$ at a fixed wait time near 2 ms for the two radial modes (dashed green and dotted purple curves for the X and Y modes, respectively), revealing slow shot-to-shot drifts. Gray bars indicate the number of shots in each 2-s time bin. Inset: Ramsey signal versus wait time near 2 ms; the wait time is chosen near $P_1 \approx 0.5$ to maximize sensitivity to small frequency shifts.

References

1. Hahn, E. L. Spin echoes. *Phys. Rev.* **80**, 580–594, DOI: <https://doi.org/10.1103/PhysRev.80.580> (1950).
2. Carr, H. Y. & Purcell, E. M. Effects of diffusion on free precession in nuclear magnetic resonance experiments. *Phys. Rev.* **94**, 630–638, DOI: <https://doi.org/10.1103/PhysRev.94.630> (1954).
3. Johansson, J. R., Nation, P. D. & Nori, F. QuTiP 2: a Python framework for the dynamics of open quantum systems. *Comput. Phys. Commun.* **184**, 1234–1240, DOI: <https://doi.org/10.1016/j.cpc.2012.11.019> (2013).